

# Super-Resolution Optical Measurement of Nanoscale Photoacid Distribution in Lithographic Materials

Adam J. Berro,<sup>1</sup> Andrew J. Berglund,<sup>1</sup> Peter T. Carmichael,<sup>1</sup> Jong Seung Kim,<sup>2</sup> J. Alexander Liddle<sup>1\*</sup>

<sup>1</sup>Center for Nanoscale Science and Technology, National Institute of Standards and Technology, Gaithersburg, MD 20899

<sup>2</sup>Department of Chemistry, Korea University, Seoul 136-701, Korea

## Abstract

We demonstrate a method using photoactivation localization microscopy (PALM) in a soft-material system, with a rhodamine-lactam dye that is activated both by ultraviolet light and protonation, to reveal the nanoscale photoacid distribution in a model photoresist. Chemically amplified resists are the principal lithographic materials used in the semiconductor industry. The photoacid distribution generated upon exposure and its subsequent evolution during post-exposure bake is a major limiting factor in determining the resolution and lithographic quality of the final, developed resist image. Our PALM data sets resolve the acid distribution in a latent image with sub-diffraction limit accuracy. Our overall accuracy is currently limited by residual mechanical drift.

*Keywords: single-molecule fluorescence, super-resolution microscopy, chemically-amplified resist, lithography, photoacid*

Single-molecule fluorescence imaging<sup>1</sup> has proven an incredibly powerful technique in the world of biology, with numerous advances arising as a result of the dramatically improved resolution that it offers. However, it has seen only limited application to materials science problems.<sup>2-4</sup> Here we use a novel, dual switching-mechanism dye combined with an image inversion process, and a maximum-likelihood-based image reconstruction technique as a quantitative means of probing the distribution of protons in a thin (~ 100 nm thick), lithographically-patterned polymer film. Our method permits the use of a low sampling-density of fluorophores and is generally applicable to those classes of materials possessing well-defined morphologies and enables information to be extracted while using minimally-perturbative dye loadings.

The lithographically patterned polymer film employed in this work is a model system that mimics the types of photoresists used in integrated circuit manufacturing. Today's production photoresists use chemical amplification (CA),<sup>5-6</sup> whereby each activated photoacid generator (PAG) molecule<sup>7</sup> catalyzes the removal of multiple protecting groups from the photoresist polymer backbone (Figure 1). A single photon is therefore responsible for rendering a significant volume of the resist soluble in the developer, dramatically increasing the resist's photospeed and enabling the use of lower-brightness, short-wavelength sources.<sup>8</sup> Because of the reaction-diffusion nature of the catalytic process, however, an improvement in the sensitivity (S) comes at the expense of resolution (R) and line edge roughness (LER, L). The struggle to optimize all three

parameters simultaneously is known as the RLS tradeoff, and has required a considerable amount of effort, devoted to understanding each step of the exposure and development process, in order to satisfy both the demand for both higher throughput and smaller features.<sup>9</sup>

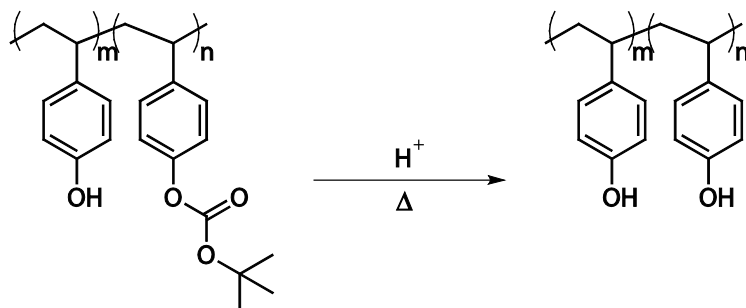


**Figure 1. Photoacid-catalyzed deprotection reaction in prototypical chemically amplified resist material.**

The lithographic process consists of four steps: (1) optical image formation, (2) interaction of the incident radiation with the PAG to create photoacid, (3) acid diffusion and deprotection of the resist polymer during a post exposure bake (PEB) of the resist to create a latent image, and (4) development of the latent image to produce the final resist features. The acid distribution is degraded relative to the optical image by a number of processes, including scattering of the incident radiation in the resist film, and diffusion of the released acid during the PEB. This degradation is captured by a single parameter, the so-called acid blur, which quantifies the standard deviation of the acid distribution (typically < 100 nm). The optical image incident on the resist can be measured and calculated precisely,<sup>10-11</sup> the extent of the deprotection reaction can be determined *via* coherent anti-Stokes Raman spectroscopy,<sup>12</sup> scanning transmission x-ray microscopy,<sup>13</sup> near-field infrared microscopy<sup>14</sup> and infrared absorbance<sup>15-16</sup> and x-ray or neutron scattering<sup>17-18</sup> from samples with large-area, flat interfaces,<sup>19</sup> and the developed resist image can be measured in detail directly by scanning electron microscopy (SEM)<sup>20</sup> and atomic force microscopy (AFM).<sup>21-22</sup> Although indirect techniques have been developed to measure an effective resist point-spread function,<sup>23</sup> the direct measurement of the photoacid distribution, and hence its influence on the resist blur, generated by the initial exposure and increased by the PEB, has proven extremely difficult. Here we demonstrate an approach using photoactivation localization microscopy (PALM) that reveals the nanoscale acid distribution created by a lithographic exposure, and its evolution during the PEB step.

This information can be used to provide insights into how the incoming radiation interacts with the resist to produce the photoacid, how photoacid and base quencher interact and how acid behaves in a realistic 3D geometry compared to the planar systems predominantly used. In addition, it is desirable to know how the acid interacts with the various components of a given resist formulation. Practically, this is most often determined by examining developed images as a function of formulation, *i.e.* the resist itself is used as the detector. However, in many cases, useful information could be obtained by, for example, observing acid behavior in individual resist components that cannot be developed. Our technique enables this type of measurement.

Fluorescence techniques have been used previously to quantify aspects of photoacid behavior such as quantum yield<sup>24</sup> and catalytic chain length in lithographically patterned thin films,<sup>25</sup> but with low degrees of spatial resolution.<sup>26</sup> Conventional fluorescence microscopy is diffraction limited (*i.e.* has a resolution limit on the order of 200 nm to 300 nm) and so is incapable of resolving the acid distribution at the relevant length scales (< 100 nm). Super-resolution single-molecule fluorescence microscopy<sup>27</sup> is a promising method for addressing this problem due to its high spatial resolution. In some of these super-resolution methods,<sup>28-30</sup> a low-dose photoactivation pulse creates a widely-spaced population of fluorescent molecules that are individually imaged and their positions determined precisely by centroiding the diffraction-limited image of each one. A super-resolution image is built up through multiple cycles of activation and imaging.

In the absence of a dye that becomes photoactive upon protonation, the use of an acid-sensitive fluorophore alone will generate a conventional fluorescence image of the exposed pattern. To achieve single-molecule, super-resolution imaging, we use a dye that can be activated either by UV illumination or protonation.<sup>31-32</sup> Exposure of the PAG generates acid that protonates all of the dye present in the patterned regions. This population is subsequently photobleached prior to PALM imaging of the remaining dye molecules in the unexposed regions which gives the inverse image of the original exposure (Figure 2).

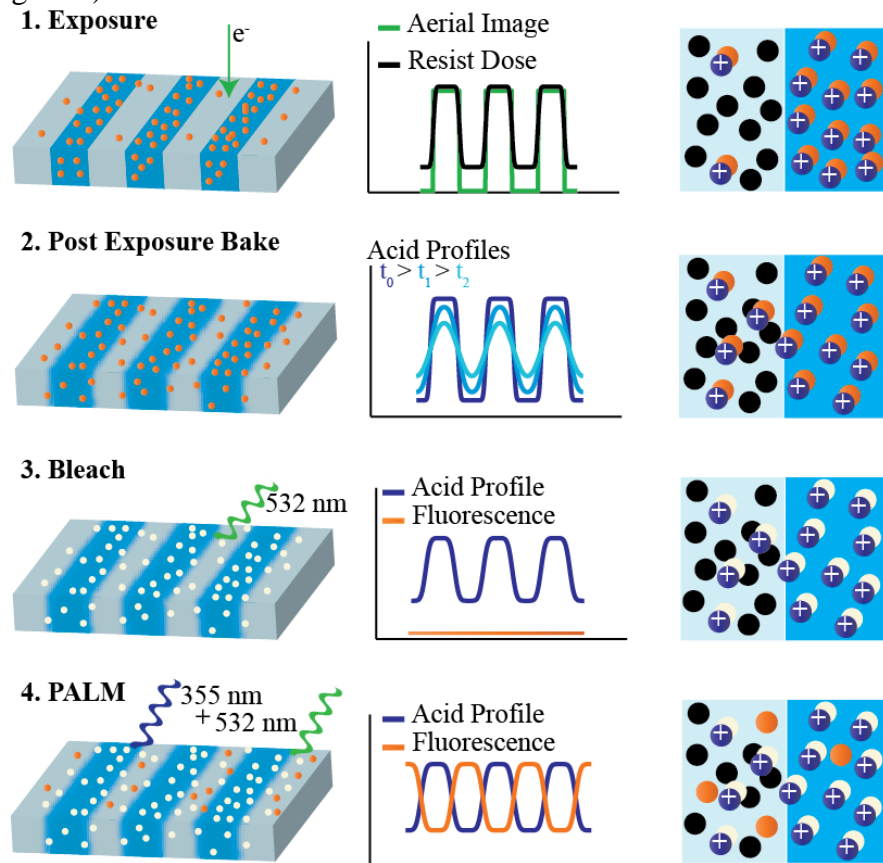


**Figure 2. Experiment process flow.** For each step we show a perspective view of sample (left), probability distributions for key components (middle), and more detailed top-down schematic illustrating various states of

the fluorophore (right). (1) Radiation incident from the aerial image (in our case, electrons) generates initial acid distribution in resist film. Protonation of unactivated fluorophores (black) renders them fluorescent (orange). (2) Diffusion blurs the initial acid profile during the post exposure bake resulting in protonation and activation of fluorophores outside the initial exposure areas. (3) Proton-activated fluorophores bleached from extended exposure to 532 nm light. (4) PALM data set collected by repeated cycles of 355 nm photoactivation followed by 532 nm fluorescence imaging of sparsely spaced fluorophores. Statistical analysis of data sets reveals acid distribution.

Current lithographic exposures generate sub-100 nm features with LER of  $< 10$  nm. In order to image an arbitrary 2D structure using PALM to a resolution of 10 nm, the largest average fluorophore spacing that can be used according to the Nyquist criterion,<sup>33</sup> is approximately half the desired resolution. This is equivalent to 40 000 fluorophores per square micrometer. Using such high concentrations is precluded because the fluorophores will interact - either by aggregating or quenching one another<sup>34</sup> - and also will perturb the behavior of the photoresist.<sup>35</sup> We circumvent this concentration limit by exposing a *structured* (non-arbitrary) pattern - a grating - that allows for integration of the data over one of the dimensions. Because of this condition, we can obtain nanoscale acid distribution information even when we employ a fluorophore concentration that is orders of magnitude below that required by the Nyquist limit for an arbitrary pattern.

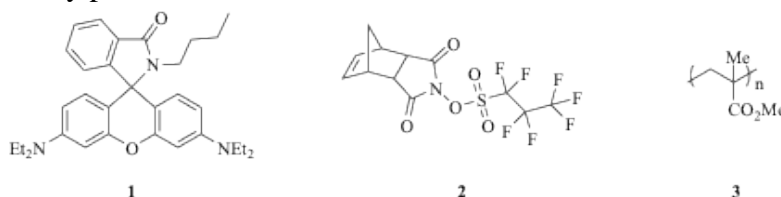


Figure 3. Rhodamine dye, PAG, and host polymer structures.

We use a model resist film 100 nm thick, spin-coated from a propylene glycol methyl ether acetate solution consisting of PMMA (0.04 mass fraction, 4 wt%) and a nonionic PAG **2** (0.01 mass fraction), which releases photoacid upon electron-beam or optical exposure below 260 nm (here we use electron-beam exposures). A bright, photostable, hydrophobic, rhodamine-lactam fluorophore (**1**) (Figure 4,  $\lambda_{\text{ex}} = 550$  nm,  $\lambda_{\text{em}} = 579$  nm. See Figure 1 of Supporting Information (SI) for more details) is mixed into the resist formulation at a number density of  $28 \mu\text{m}^{-3}$  before use.

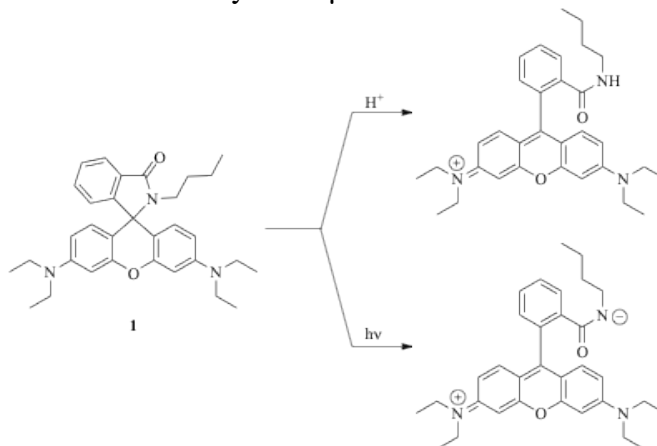


Figure 4. Activation of Rhodamine dye via protonation and UV excitation pathways.

The ratio of PAG to fluorophore in solution is 480:1 and the resulting number of fluorophores observed in the patterned area totals between 7 000 and 13 000. In our experiments a typical PALM cycle comprises a 30 ms to 40 ms 355 nm photoactivation exposure ( $\approx 0.14 \text{ W/cm}^2$  to  $3.5 \text{ W/cm}^2$ ), followed by an image acquisition sequence of 10 s under 532 nm light ( $\approx 353 \text{ W/cm}^2$ ), of 100 frames of 100 milliseconds each. In each cycle, an image of gold fiducial marks is collected using illumination from an 850 nm light-emitting diode and is used to register subsequent images to one another. Each fluorophore appears as a diffraction limited spot containing  $\approx 10\,000$  photons [see Supporting Information for details], and is localized using the “Gaussian mask” centroiding algorithm.<sup>36</sup> In a typical experiment we collect 60 cycles for a total number of fluorophores ranging from 1 000 to 4 000 within the  $400 \mu\text{m}^2$  electron-beam patterned area (see SI for more details).

Quantitative information and qualitative pattern estimates can be extracted from the data using a maximum likelihood estimator (MLE) that incorporates our prior knowledge of the exposure geometry and fluorophore activation process. In effect, by using a sparse set of data points, we can extract information with spatial resolution significantly better than the inter-fluorophore spacing. The electron exposure profile is an equal line-space pattern with adjustable line width  $d$  and fixed contrast  $c=0.72$ ,<sup>37</sup> whereas the blur associated with the resulting acid profile is modeled by convolving the pattern with a Gaussian function of width (standard deviation)  $\sigma$ . This “blurred square-wave” pattern  $g(x,y)$  represents the acid distribution at each position; the local density of fluorophores  $f(x,y)$  that survive a subsequent bleach step is given by the exponential of this function:  $f(x,y) = f_0 \exp[-\alpha g(x,y)]$  where  $\alpha$  is a “saturation parameter” that summarizes the efficiency of fluorophore activation by electron irradiation followed by local photoacid generation and  $f_0$  is a normalization constant. An overall rotation angle  $\phi$  and pattern offset  $\delta x$  are also adjustable parameters. Collecting all parameters  $d$ ,  $\alpha$ ,  $\phi$ ,  $\delta x$ , and  $\sigma$  into a vector  $\theta$ , we can denote the two-dimensional model function by  $f(x,y|\theta)$  representing the acid distribution. For any measured data set consisting of  $N$  fluorophores at locations  $(x_i, y_i)$  with  $i=1 \dots N$ , we form a likelihood function for the PALM data:

$$L(\theta) = \sum_{i=1}^N \log f(x_i, y_i | \theta)$$

The maximum likelihood estimate of the acid distribution parameters is given by the value of  $\theta$  that maximizes  $L(\theta)$ . Using this parameter estimation procedure, we can estimate the acid distribution from the PALM data, and visualize it as in Figures 5 and 6, which show the raw PALM data (a) and the resulting effective modulation transfer function (b).

## Results and Discussion

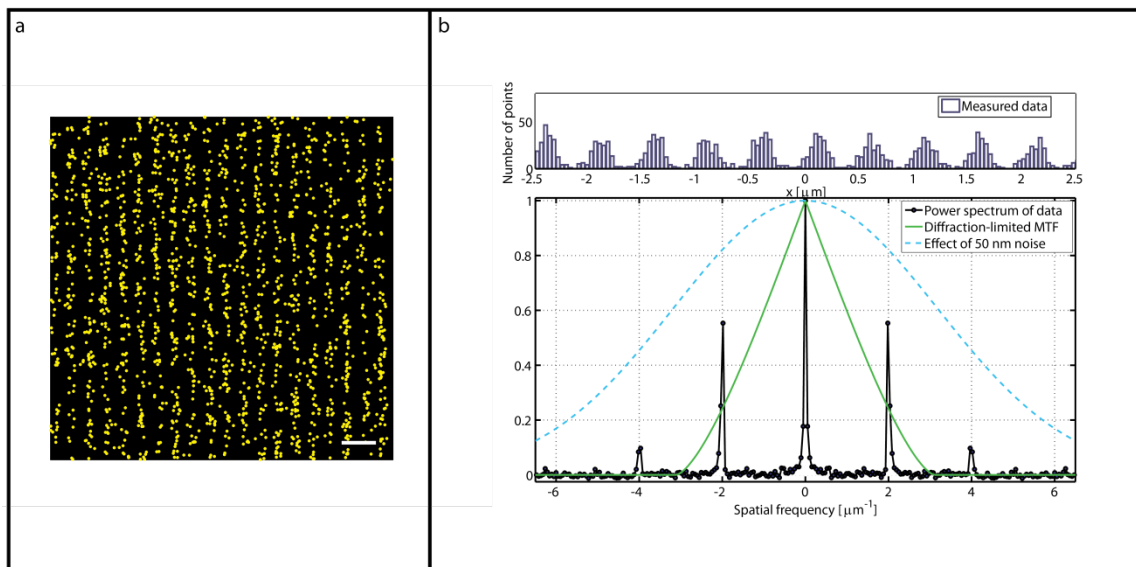


Figure 5. a) Raw PALM data. Each point represents one localized fluorophore. Scale bar is  $1 \mu\text{m}$ . b) Normalized power spectrum of PALM data from a developed sample containing fluorophore only. Upper panel shows a histogram of PALM data along the pattern direction (integrated over  $y$ ). Lower panel shows the observed power spectrum of the PALM data, with very well-resolved peaks at the pattern period  $2 \mu\text{m}^{-1} = 1/(500 \text{ nm})$  and the first harmonic  $4 \mu\text{m}^{-1} = 1/(250 \text{ nm})$ . The solid green line is the modulation transfer function (MTF) of a diffraction-limited microscope with numerical aperture ( $\text{NA}=0.9$ ) and peak emission wavelength ( $\lambda=579 \text{ nm}$ ) corresponding to our instrument.<sup>38</sup> For traditional imaging, there is no information content beyond  $3.1 \mu\text{m}^{-1} \approx 1/(320 \text{ nm})$ . For PALM imaging, noise sources contribute a Gaussian low-pass filter on the power spectrum; an example is shown in the figure for  $50 \text{ nm}$  noise. As in traditional imaging,<sup>39</sup> the ultimate resolution is determined by the noise level set here by the number  $N$  of observed fluorophores.

The *developed* features imaged in Figure 5 consist effectively of sharp-edged top-hat functions and therefore contain very high spatial frequencies. As such, they act as a resolution test structure. Using these, we note from repeated experiments, at the signal-to-noise levels currently attainable, that spatial frequencies of  $5 \mu\text{m}^{-1}$  and above are attenuated beyond resolution. We attribute this result to noise at the level of  $50 \text{ nm}$ , which will attenuate those spatial frequencies by at least 70 %. The dashed curve in Figure 5 shows the attenuation factor as a function of spatial frequency that would result from a  $50 \text{ nm}$  standard deviation Gaussian noise on each fluorophore location. Possible sources of this noise include: imperfect drift/focus correction, incomplete rejection of signals from overlapping fluorophores,<sup>40</sup> and molecular tilt and defocus of fluorophores.<sup>41</sup> These can all be mitigated by improved system design<sup>42</sup> and data analysis.<sup>43-44</sup>

Acid distributions in *undeveloped* samples are inferred from the observed fluorophore distributions (which correspond to the *inverse* of the acid distribution) using the MLE described above.

Acid diffusion during the PEB step was determined by heating wafers containing line and space patterns with a period of  $500 \text{ nm}$  ( $2 \mu\text{m}^{-1}$ ) to  $90 \text{ }^\circ\text{C}$  for varying lengths of time. This temperature was chosen to keep the polymer below the glass transition of the matrix (Bulk  $T_g$   $105 \text{ }^\circ\text{C}$ ), consistent with standard procedures employed in the semiconductor industry. We observe that the best-fit (maximum likelihood) profiles show decreasing contrast and increasing edge slopes with longer bake times. We believe this to be caused by the movement of acid in the film, as would be expected (Figure 6).

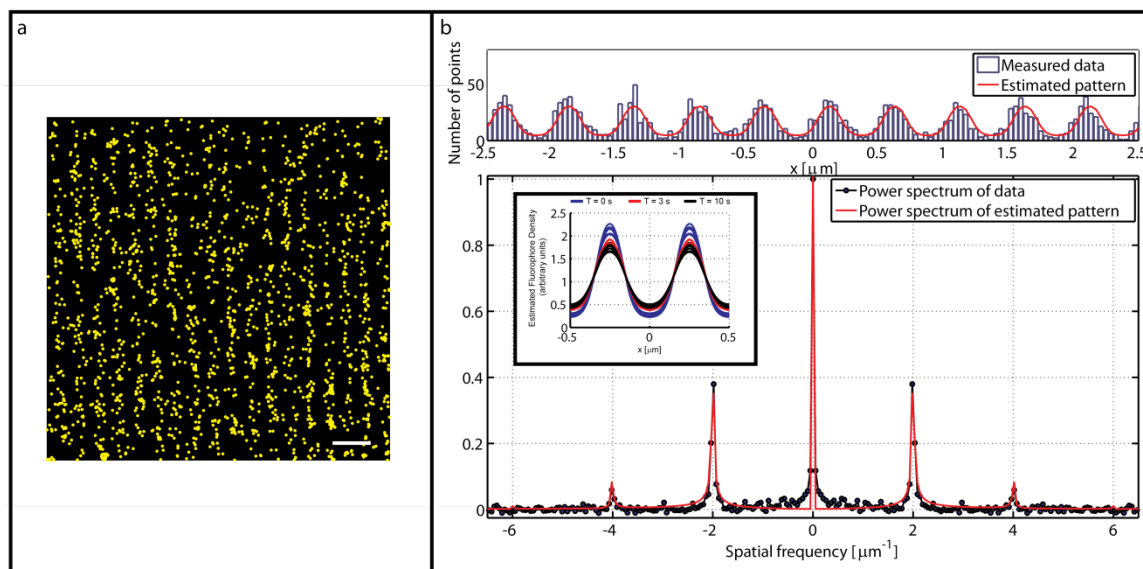


Figure 6. a) Raw PALM data. Each point represents one localized fluorophore. Scale bar is  $1 \mu\text{m}$ . b) PALM acid distribution data from an undeveloped sample. Upper panel shows a histogram of PALM data along the pattern direction (integrated over  $y$ ). Lower panel shows the observed power spectrum of the PALM data, with very well-resolved peaks at the pattern period  $2 \mu\text{m}^{-1} = 1/(500 \text{ nm})$  and the first harmonic  $4 \mu\text{m}^{-1} = 1/(250 \text{ nm})$ . The inset shows best-fit profiles from multiple samples with no processing (blue) and samples subjected to post-exposure bake at  $90^\circ \text{C}$  for 3 s (red) and 10 s (black). Each curve represents the fit for an individual sample.

## Conclusion

Our results show that single-molecule, super-resolution microscopy with an acid-sensitive, photo-activatable dye, can be used to reveal the nanoscale distribution of photoacid in chemically-amplified resist materials. Our current instrument is limited by noise sources to approximately  $50 \text{ nm}$ , but there is no fundamental reason that the resolution cannot be improved to the  $20 \text{ nm}$  level or beyond.<sup>45</sup> The combination of a lithographically defined pattern and maximum-likelihood analysis allows us to extract information and estimate profiles at very low fluorophore loadings. This new technique completes the suite of tools needed for a complete understanding of the lithographic process, and will permit improved optimization of resist materials for advanced patterning. Modification of the rhodamine-based dye to red-shift the photoactivation wavelength away from the absorbance of arylsulfonium and arylodonium salts would allow this method to be used on production  $248 \text{ nm}$  or  $193 \text{ nm}$  photoresists and allow for comparison with subsequently developed resist features. The method introduced here may also have applications in imaging acid and ion distributions in other nanoscale functional materials, such as lithium-ion batteries, proton exchange membranes, and block copolymers. Finally, we note that, in contrast to the biological domain, in many materials systems it is possible to generate structured samples with a defined basis: this enables the use of sparse sampling methods to extract relevant parameters at very low fluorophore loadings, or with small numbers of points in a given time period. This latter feature will be useful for dynamic studies.

## Acknowledgments

The authors would like to acknowledge Gregg Gallatin for helpful discussions, Henri Lezec for focused ion beam milling, and Jeff Fagan for assistance with fluorometry data. This work was supported by a grant from the CRI project (2011-0000420) of KRF (JSK). AJ Berro would like to thank the National Research Council for postdoctoral funding.

**Supporting Information Available:** Plots of fluorescence from activated fluorophores, resist profile from developed resist, and more detailed information on data analysis can be downloaded online. This material is available free of charge *via* the Internet at <http://pubs.acs.org>.

## Experimental

**Resist Formulation** Resist for development was formulated using 40 mg of 350 000 MW poly(methylmethacrylate) (PMMA) dissolved into 960 mg of propylene glycol monomethyl ether acetate (PGMEA). 15  $\mu\text{L}$  of rhodamine dye solution (3 mmol/L in PGMEA) was added to the above solution, which was then stirred to ensure proper mixing.

Resist samples for imaging without development were formulated using 40 mg of 350 000 MW PMMA, 10 mg of *N*-hydroxy-5-norbornene-2,3-dicarboximide perfluoro-1-butanesulfonate, and 950 mg of PGMEA, to which 15  $\mu\text{L}$  of rhodamine dye solution (3 mmol/L in PGMEA) was added.

**Spin Coating and Exposure** The solutions were spin-coated at  $400 \text{ rad s}^{-1}$  (4 000 rpm) for 60 s and then subjected to a post-apply bake for 60 s at  $95 \text{ }^\circ\text{C}$ . The final film thickness was  $\approx 100 \text{ nm}$  as measured by profilometry. The undeveloped resist was patterned by electron-beam exposure ( $500 \text{ } \mu\text{C}/\text{cm}^2$  to  $700 \text{ } \mu\text{C}/\text{cm}^2$  dose at 100 kV) and used without further processing. The developed sample was patterned using electron-beam exposure ( $500 \text{ } \mu\text{C}/\text{cm}^2$  dose at 100 kV) and developed by immersion using a mixture of methyl isobutyl ketone and isopropanol (with volume fractions of 0.17 and 0.83, respectively) for 180 s. See Supporting Information for a cross-section image of developed features.

**PALM Microscopy** The wafer was then placed into a metrology microscope outfitted for epifluorescence microscopy and illuminated using a 532 nm diode-pumped solid state (DPSS) continuous wave laser for 45 min (this was the time needed to bleach the initial population of active fluorophores to an intensity level near the background). Exposure cycles during the experiment consisted of 355 nm illumination for 60 ms through a neutral density filter ( $\approx 0.14 \text{ W}/\text{cm}^2$ ) followed by 532 nm illumination for 10 s ( $\approx 353 \text{ W}/\text{cm}^2$ ). During 532 nm illumination, images were collected using a 100X 0.9NA objective and a back illuminated electron-multiplying charge couple device (EMCCD) camera (cooled to  $-80 \text{ }^\circ\text{C}$ , 300 X electron multiplication) in 100 ms frames. This process was controlled by a pulse generator (triggering shutter controllers for laser switching) and an arbitrary function generator (for camera frame capture trigger). In all experiments, 60 cycles were collected (6000 frames).



**Data Analysis** Data was analyzed using a custom code to combine all frames from each cycle, reject overlapping fluorophores and to plot fluorophore positions. A separate code was then used to fit the line-and-space pattern to each data set. Further details can be found in the Supporting Information.

## References

1. Moerner, W. E., Microscopy beyond the diffraction limit using actively controlled single molecules. *J. Microsc.* **2012**, *246*, 213-220.
2. Aoki, H.; Mori, K.; Ito, S., Conformational analysis of single polymer chains in three dimensions by super-resolution fluorescence microscopy. *Soft Matter* **2012**, *8*, 4390-4395.
3. Bolinger, J. C.; Traub, M. C.; Adachi, T.; Barbara, P. F., Ultralong-Range Polaron-Induced Quenching of Excitons in Isolated Conjugated Polymers. *Science* **2011**, *331*, 565-567.
4. Woll, D.; Braeken, E.; Deres, A.; De Schryver, F. C.; Uji-i, H.; Hofkens, J., Polymers and single molecule fluorescence spectroscopy, what can we learn? *Chem. Soc. Rev.* **2009**, *38*, 313-328.
5. Wallraf, G. M.; Hinsberg, W. D., Lithographic Imaging Techniques for the Formation of Nanoscopic Features. *Chem. Rev.* **1999**, *99*, 1801-1821.
6. Sanders, D. P., Advances in Patterning Materials for 193 nm Immersion Lithography. *Chem. Rev.* **2010**, *110*, 321-360.
7. Crivello, J. V., The Discovery and Development of Onium Salt Cationic Photoinitiators. *J. Polym. Sci., Part A: Polym. Chem.* **1999**, *37*, 4241-4254.
8. Willson, C. G.; Ito, H.; Frechet, J. M. J.; Tessier, T. G.; Houlihan, F. M., Approaches to the Design of Radiation-Sensitive Polymeric Imaging Systems with Improved Sensitivity and Resolution. *J. Electrochem. Soc.* **1986**, *133*, 181-187.
9. Gallatin, G. M., Resist Blur and Line Edge Roughness. *Proc. SPIE* **2005**, *5754*, 38-52.
10. Mack, C. A., In *Fundamental Principles of Optical Lithography*, John Wiley & Sons Inc.: Hoboken, NJ, 2007; pp 25-125.
11. Wong, A. K. K., In *Resolution Enhancement Techniques in Optical Lithography*, SPIE Press: Bellingham, WA, 2001; pp 31-180.
12. Potma, E. O.; Xie, X. S.; Muntean, L.; Preusser, J.; Jones, D.; Ye, J.; Leone, S. R.; Hinsberg, W. D.; Schade, W., Chemical Imaging of Photoresists with Coherent Anti-Stokes Raman Scattering (CARS) Microscopy. *J. Phys. Chem. B* **2003**, *108*, 1296-1301.
13. Muntean, L.; Planques, R.; Kilcoyne, A. L. D.; Leone, S. R.; Gilles, M. K.; Hinsberg, W. D., Chemical mapping of polymer photoresists by scanning transmission x-ray microscopy. *J. Vac. Sci. Technol. B.* **2005**, *23*, 1630-1636.
14. Dragnea, B.; Preusser, J.; Szarko, J. M.; McDonough, L. A.; Leone, S. R.; Hinsberg, W. D., Chemical mapping of patterned polymer photoresists by near-field infrared microscopy. *Appl. Surf. Sci.* **2001**, *175-176*, 783-789.

15. Kang, S.; Wu, W.-I.; Choi, K.-W.; De Silva, A.; Ober, C. K.; Prabhu, V. M., Characterization of the Photoacid Diffusion Length and Reaction Kinetics in EUV Photoresists with IR Spectroscopy. *Macromolecules* **2010**, *43*, 4275-4286.
16. Schmid, G. M.; Stewart, M. D.; Wang, C.-Y.; Vogt, B. D.; Prabhu, V. M.; Lin, E. K.; Willson, C. G., Resolution limitations in chemically amplified photoresist systems. *Proc. SPIE* **2004**, *5376*, 333-342.
17. Vogt, B. D.; Kang, S.; Prabhu, V. M.; Lin, E. K.; Satija, S. K.; Turnquest, K.; Wu, W.-L., Measurements of the Reaction-Diffusion Front of Model Chemically Amplified Photoresists with Varying Photoacid Size. *Macromolecules* **2006**, *39*, 8311-8317.
18. Lin, E. K.; Soles, C. L.; Goldfarb, D. L.; Trinque, B. C.; Burns, S. D.; Jones, R. L.; Lenhart, J. L.; Angelopoulos, M.; Willson, C. G.; Satija, S. K.; Wu, W.-L., Direct Measurement of the Reaction Front in Chemically Amplified Photoresists. *Science* **2002**, *297*, 372-375.
19. Prabhu, V. M.; Kang, S. H.; VanderHart, D. L.; Satija, S. K.; Lin, E. K.; Wu, W. L., Photoresist Latent and Developer Images as Probed by Neutron Reflectivity Methods. *Adv. Mater.* **2011**, *23*, 388-408.
20. Vladar, A. E.; Postek, M. T., Scanning Electron Microscope. In *Handbook of Charged Particle Optics, 2nd. Ed.*, CRC Press: Rockaway Beach, OR, 2008; pp 437-496.
21. Orji, N. G.; Dixson, R. G.; Martinez, A.; Bunday, B. D.; Allgair, J. A.; Vorburger, H. V., Progress on implementation of a reference measurement system based on a critical-dimension atomic force microscope. *J. Micro-Nanolithogr. MEMS MOEMS* **2007**, *6*, 023002.
22. Kramar, J. A.; Dixson, R.; Orji, N. G., Scanning probe microscope dimensional metrology at NIST. *Meas. Sci. Technol.* **2011**, *22*, 024001.
23. Hoffnagle, J. A.; Hinsberg, W. D.; Sanchez, M. I.; Houle, F. A., Method of measuring the spatial resolution of a photoresist. *Opt. Lett.* **2002**, *27*, 1776-1778.
24. Ray, K.; Mason, M. D.; Grober, R. D.; Pohlars, G.; Staford, C.; Cameron, J. F., Quantum Yields of Photoacid Generation in 193-nm Chemically Amplified Resists by Fluorescence Imaging Spectroscopy. *Chem. Mater.* **2004**, *16*, 5726-5730.
25. Frenette, M.; Ivan, M. G.; Scaiano, J. C., Use of fluorescent probes to determine catalytic chain length in chemically amplified resists. *Can. J. Chem.* **2005**, *83*, 869-874.
26. Bukofsky, S. J.; Feke, G. D.; Wu, Q.; Grober, R. D.; Dentinger, P. M.; Taylor, J. W., Imaging of photogenerated acid in a chemically amplified photoresist. *Appl. Phys. Lett.* **1998**, *73*, 408-410.
27. Hell, S. W., Far-Field Optical Nanoscopy. *Science* **2007**, *316*, 1153-1158.
28. Betzig, E.; Patterson, G. H.; Sougrat, R.; Lindwasser, O. W.; Olenych, S.; Bonifacino, J. S.; Davidson, M. W.; Lippincott-Schwartz, J.; Hess, H. F., Imaging intracellular fluorescent proteins at nanometer resolution. *Science* **2006**, *313*, 1642-1645.
29. Hess, S. T.; Girirajan, T. P. K.; Mason, M. D., Ultra-High Resolution Imaging by Fluorescence Photoactivation Localization Microscopy. *Biophys. J.* **2006**, *91*, 4258-4272.

30. Rust, M. J.; Bates, M.; Zhuang, X., Sub-diffraction-limit imaging by stochastic optical reconstruction microscopy (STORM). *Nat. Methods* **2006**, *3*, 793-795.
31. Kim, H. N.; Lee, M. H.; Kim, H. J.; Kim, J. S.; Yoon, J., A new trend in rhodamine-based chemosensors: application of spirolactam ring-opening to sensing ions. *Chem. Soc. Rev.* **2008**, *37*, 1465-1472.
32. Quang, D. T.; Kim, J. S., Fluoro- and Chromogenic Chemodosimeters for Heavy Metal Ion Detection in Solution and Biospecimens. *Chem. Rev.* **2010**, *110*, 6280-6301.
33. Shannon, C. E., Communication in the Presence of Noise. *Proc. IRE* **1949**, *37*, 10-21.
34. Imhof, A.; Megens, M.; Engelberts, J. J.; de Lang, D. T. N.; Sprik, R.; Vos, W. L., Spectroscopy of Fluorescein (FITC) Dyed Colloidal Silica Spheres. *J. Phys. Chem. B* **1999**, *103*, 1408-1415.
35. MacDonald, S. A.; Hinsberg, W. D.; Wendt, H. R.; Clecak, N. J.; Willson, C. G.; Snyder, C. D., Airborne Contamination of Chemically Amplified Resist. 1. Identification of Problem. *Chem. Mater.* **1993**, *5*, 348-356.
36. Thompson, R. E.; Larson, D. R.; Webb, W. W., Precise Nanometer Localization Analysis for Individual Fluorescent Probes. *Biophys. J.* **2002**, *82*, 2775-2783.
37. Watson, G. P.; Berger, S. D.; Liddle, J. A.; Fetter, L. A.; Farrow, R. C.; Tarascon, R. G.; Mkrtchyan, M.; Novembre, A. E.; Blakey, M. I.; Bolan, K. J.; Poli, L., Precise measurement of the effective backscatter coefficient for 100-keV electron-beam lithography on Si. *J. Vac. Sci. Technol., B* **1995**, *13*, 2535-2538.
38. Goodman, J. W., Frequency Analysis of Optical Imaging Systems. In *Introduction to Fourier Optics*, Roberts & Company: Englewood, CO, 2005; pp 127-172.
39. Cox, I. J.; Sheppard, C. J. R., Information Capacity and Resolution in an Optical System. *J. Opt. Soc. Am. A* **1986**, *3*, 1152-1158.
40. Small, A. R., Theoretical Limits on Errors and Acquisition Rates in Localizing Switchable Fluorophores. *Biophys. J.* **2009**, *96*, L16-L18.
41. Engelhardt, J.; Keller, J.; Hoyer, P.; Reuss, M.; Staudt, T.; Hell, S. W., Molecular Orientation Affects Localization Accuracy in Superresolution Far-Field Fluorescence Microscopy. *Nano Lett.* **2011**, *11*, 209-213.
42. Lee, S. H.; Baday, M.; Tjioe, M.; Simonson, P. D.; Zhang, R.; Cai, E.; Selvin, P. R., Using fixed fiduciary markers for stage drift correction. *Opt. Express* **2012**, *20*, 12177-12183.
43. Holden, S. J.; Uphoff, S.; Kapanidis, A. N., DAOSTORM: an algorithm for high-density super-resolution microscopy. *Nat. Methods* **2011**, *8*, 279-280.
44. Zhu, L.; Zhang, W.; Elnatan, D.; Huang, B., Faster STORM using compressed sensing. *Nat. Methods* **2012**, *9*, 721-723.
45. Xu, K.; Babcock, H. P.; Zhuang, X. W., Dual-objective STORM reveals three-dimensional filament organization in the actin cytoskeleton. *Nat. Methods* **2012**, *9*, 185-188.